

Infrared Universality: The r^{-3} Spectral Threshold for Coupled Gravitational and Electromagnetic Fields

Michael Wilson

University of Arkansas at Little Rock

November 13, 2025

Abstract

We identify the r^{-3} curvature-decay rate as a universal geometric threshold separating compact from non-compact perturbations of Laplace-type operators on asymptotically flat manifolds. For the coupled Einstein–Maxwell system, we prove that the linearized operator \mathcal{L} is essentially self-adjoint and that curvature and field strengths decaying faster than r^{-3} act as relatively compact perturbations, while decay exactly at r^{-3} places $0 \in \sigma_{\text{ess}}(\mathcal{L})$ through delocalized zero modes. This threshold mechanism unifies the infrared behavior of spin-1, spin-2, and mixed spin- $(1 \oplus 2)$ fields, linking the onset of spectral delocalization with the appearance of gravitational and electromagnetic memory. Finite-difference simulations corroborate the analytic scaling and reproduce the characteristic quadrupolar and dipolar sky maps predicted for the coupled memory fields. These results demonstrate that curvature decay at r^{-3} constitutes a fundamental geometric boundary underlying infrared universality in gauge and gravitational theories, providing a spectral counterpart to the asymptotic-symmetry and soft-theorem formulations of memory.

1 Introduction

The long-range structure of classical gauge and gravitational fields is governed by the interplay between curvature decay and spectral stability. In asymptotically flat spacetimes, the Laplace-type operators governing linearized perturbations acquire nontrivial essential spectra when the background curvature decays too slowly at infinity. For scalar Schrödinger operators this transition is well understood: potentials decaying faster than r^{-2} are relatively compact perturbations, while those with r^{-2} or slower decay alter the continuous spectrum. The analogous boundary for tensorial or gauge-covariant operators, however, remains less clearly defined.

Recent analyses of the non-Abelian Laplacian [20] and the linearized Einstein operator [21] revealed that a decay rate of $|\text{Riem}^{(0)}| \sim r^{-3}$ marks the critical threshold at which delocalized zero modes first appear. This r^{-3} scaling corresponds geometrically to the leading falloff of the Riemann tensor generated by an isolated mass and, physically, to the onset of the memory effect in radiative solutions. While the spectral effects of r^{-3} potentials are classically known, this work establishes that curvature decay at precisely this rate defines a *universal infrared boundary* for massless fields in four dimensions. We demonstrate that this geometric mechanism governs

the transition between localized and delocalized modes across spin-1, spin-2, and coupled spin- $(1 \oplus 2)$ systems, supported by explicit Weyl-sequence constructions and numerical verification of the sharp threshold.

The analysis proceeds in three parts. Section II formulates the coupled Einstein–Maxwell system on an asymptotically flat background and defines the linearized operator \mathcal{L} acting on the combined metric–vector perturbation (h_{ij}, a_i) . Section III establishes self-adjointness and determines the stability of the essential spectrum under gauge projection, proving that curvature and field strengths with decay r^{-p} are relatively compact perturbations of the flat Laplacian for $p > 3$, but not for $p \leq 3$. Section IV constructs explicit Weyl sequences demonstrating that $0 \in \sigma_{\text{ess}}(\mathcal{L})$ when $p = 3$, and Section V presents finite-difference simulations confirming the analytic scaling and the associated angular structure of the gravitational and electromagnetic memory fields.

The results indicate that the r^{-3} curvature-decay rate constitutes a geometric threshold separating compact from non-compact perturbations of Laplace-type operators. This threshold unifies the infrared structure of gauge and gravitational theories through a common spectral mechanism, suggesting that classical memory effects represent the physical manifestation of this spectral transition.

2 Preliminaries

We work on a three-dimensional, asymptotically flat Riemannian manifold $(\Sigma, g^{(0)})$ arising as a spatial slice of an Einstein–Maxwell background $(\mathcal{M}, g_{\mu\nu}^{(0)}, F_{\mu\nu}^{(0)})$ satisfying

$$G_{\mu\nu}[g^{(0)}] = 8\pi T_{\mu\nu}^{(\text{EM})}[F^{(0)}], \quad \nabla^\mu F_{\mu\nu}^{(0)} = 0, \quad \nabla_{[\lambda} F_{\mu\nu]}^{(0)} = 0,$$

with $T_{\mu\nu}^{(\text{EM})} = F_{\mu\alpha}^{(0)} F_{\nu}^{(0)\alpha} - \frac{1}{4} g_{\mu\nu}^{(0)} F_{\alpha\beta}^{(0)} F^{(0)\alpha\beta}$. Geometric units $G = c = 1$ are used throughout.

2.1 Asymptotic structure

In global harmonic coordinates (x^i) on $\Sigma \simeq \mathbb{R}^3$ we assume

$$g_{ij}^{(0)} = \delta_{ij} + O(r^{-1}), \quad \partial_k g_{ij}^{(0)} = O(r^{-2}), \quad F_{ij}^{(0)} = O(r^{-2}), \quad \nabla_k F_{ij}^{(0)} = O(r^{-3}).$$

Hence

$$|\text{Riem}^{(0)}| = O(r^{-3}), \quad |F^{(0)}| = O(r^{-2}), \quad |\nabla F^{(0)}| = O(r^{-3}).$$

The curvature tensor therefore decays one power faster than the connection, and the electromagnetic field strength decays as r^{-2} while its derivative appears at the critical r^{-3} rate.

Remark 2.1. The critical loss of compactness is governed by the zeroth-order blocks built from $|\text{Riem}^{(0)}|$ and $|\nabla F^{(0)}|$, both $O(r^{-3})$; the first-order coefficients $b^k = O(r^{-2}) \in L^3(\mathbb{R}^3)$ remain compact after composition with $(H_0 + 1)^{-1/2}$.

The first de Rham cohomology $H_{\text{dR}}^1(\Sigma) = 0$ ensures unique Hodge decomposition and allows the Helmholtz projection onto divergence-free fields.

2.2 Regularity and gauge fixing

We assume $g^{(0)} \in C^2$ and $F^{(0)} \in C^1$ with the above asymptotics, the minimal regularity required to define curvature, $\nabla F^{(0)}$, and to apply the Sobolev–Rellich embeddings used below. Higher smoothness may be imposed without loss of generality.

Perturbations $(h_{\mu\nu}, a_\mu)$ satisfy

$$g_{\mu\nu} = g_{\mu\nu}^{(0)} + h_{\mu\nu}, \quad A_\mu = A_\mu^{(0)} + a_\mu, \quad f_{\mu\nu} = 2\nabla_{[\mu} a_{\nu]}.$$

We adopt the harmonic (de Donder) and Lorenz gauges $\nabla^\mu \bar{h}_{\mu\nu} = 0$ and $\nabla^\mu a_\mu = 0$, which on Σ impose the elliptic constraints $\nabla^j \bar{h}_{ij} = 0$ and $\nabla^i a_i = 0$.

2.3 Weighted domain and Hilbert space

Define

$$H_\delta^2(\Sigma; E) = \{u \in H_{\text{loc}}^2(\Sigma; E) : \langle r \rangle^{\delta+k} \nabla^k u \in L^2, \ k \leq 2\}, \quad \langle r \rangle = (1 + r^2)^{1/2},$$

with $E = S_0^2 T^* \Sigma \oplus T^* \Sigma$ and $-1 < \delta < 0$. The gauge–fixed space is

$$\mathcal{H}_\delta = (H_\delta^2 \cap \ker \nabla^*)(S_0^2 T^* \Sigma) \oplus (H_\delta^2 \cap \ker \nabla^*)(T^* \Sigma),$$

equipped with the L^2 inner product of $g^{(0)}$. Gauge corrections are obtained from the elliptic equations $\nabla^* \nabla \xi = \nabla^j \bar{h}_{ij}$ and $\nabla^* \nabla \lambda = \nabla^i a_i$, whose unique decaying solutions exist, ensuring that projection to $\ker \nabla^*$ is well defined.

2.4 Block operator and off–diagonal structure

The spatial operator reads

$$\mathcal{L} \begin{pmatrix} h \\ a \end{pmatrix} = \begin{pmatrix} L_{\text{grav}} h + C^\dagger a \\ Ch + L_{\text{EM}} a \end{pmatrix},$$

where

$$(L_{\text{grav}} h)_{ij} = -\nabla^k \nabla_k h_{ij} - 2R_{ikjl} h^{kl} + 2R_{(i}{}^k h_{j)k}, \quad (1)$$

$$(L_{\text{EM}} a)_i = -\nabla^k \nabla_k a_i + R_i{}^k a_k. \quad (2)$$

Explicit form of C and C^\dagger . From $\delta T_{ij}^{(\text{EM})} = F_{i\alpha}^{(0)} f_j{}^\alpha + F_{j\alpha}^{(0)} f_i{}^\alpha - \frac{1}{2} g_{ij}^{(0)} F_{\alpha\beta}^{(0)} f^{\alpha\beta} - \frac{1}{4} h_{ij} F_{\alpha\beta}^{(0)} F^{(0)\alpha\beta}$, using $f_{k\ell} = 2\nabla_{[k} a_{\ell]}$ and $\nabla^i a_i = 0$, one finds

$$(Ca)_{ij} = F_{k(i}^{(0)} \nabla^k a_{j)} - \frac{1}{2} g_{ij}^{(0)} F_{k\ell}^{(0)} \nabla^k a^\ell + (\nabla_{(i} F_{j)}^{(0)k}) a_k,$$

so that $C = b^k(x) \nabla_k + V_C(x)$ with $b^k = O(r^{-2})$, $V_C = O(r^{-3})$. Integration by parts on Σ (with decaying boundary terms) gives

$$\langle (Ca), h \rangle_{L^2} = \langle a, (C^\dagger h) \rangle_{L^2},$$

with

$$(C^\dagger h)_i = -\nabla^k \left(F_{k(i}^{(0)} h_{j)}^j - F_k^{(0)j} h_{ij} + \frac{1}{2} F_{k\ell}^{(0)} h^\ell_i \right) + (\nabla^j F_{ij}^{(0)}) h^k_k.$$

Thus \mathcal{L} is symmetric on $C_c^\infty \cap \ker \nabla^*$, with $b^k \in L^3$ and $V_C \in L^{3/2, \infty}$.

2.5 Gauge projection and compactness

Let P_{div} denote the Helmholtz projection $P_{\text{div}} = I - \nabla \Delta^{-1} \nabla^*$. Because $g_{ij}^{(0)} - \delta_{ij} = O(r^{-1})$, the difference $P_{\text{div}}^{(g^{(0)})} - P_{\text{div}}^{(\delta)}$ is a pseudodifferential operator of order -1 with decaying coefficients, hence compact $H^2 \rightarrow L^2$.

Lemma 2.2 (Compactness of the gauge–projection commutator). *Let P_{div} be the Helmholtz projector on $(\Sigma, g^{(0)})$, a classical Ψ DO of order 0 with symbol $p(x, \xi) \in S_{1,0}^0$ converging to the flat symbol as $r \rightarrow \infty$. Let $V(x)$ be a (matrix) multiplier with $V \in L^\infty(\Sigma) \cap C_{\text{loc}}^1(\Sigma)$, $\nabla V \in L^3(\Sigma)$, and $V(x) \rightarrow 0$ as $r \rightarrow \infty$. Then*

$$[P_{\text{div}}, V] : H^2(\Sigma; E) \rightarrow H^1(\Sigma; E) \quad \text{is bounded,}$$

and, moreover,

$$[P_{\text{div}}, V] : H^2(\Sigma; E) \rightarrow L^2(\Sigma; E) \quad \text{is compact.}$$

Proof. Boundedness $H^2 \rightarrow H^1$. By Ψ DO calculus, $[P_{\text{div}}, V]$ is a classical operator of order -1 with principal symbol $\sigma_{-1}([P_{\text{div}}, V])(x, \xi) = i \partial_\xi p(x, \xi) \cdot \partial_x V(x)$. Using a standard paraproduct/Coifman-Meyer commutator estimate (see, e.g., Taylor, *PDE III*, Thm. 7.1; Coifman-Meyer), one obtains on each coordinate patch

$$\|[P_{\text{div}}, V]u\|_{H^1} \lesssim \|\nabla V\|_{L^3} \|u\|_{H^2}$$

in dimension 3, where we used Sobolev $H^2 \hookrightarrow W^{1,6}$ and $H^1 \hookrightarrow L^6$. A partition of unity and the asymptotic Euclidean structure yield the global bound.

Compactness $H^2 \rightarrow L^2$. Fix a smooth cutoff χ_R equal to 1 on $\{r \leq R\}$, supported in $\{r \leq 2R\}$. Decompose

$$[P_{\text{div}}, V] = \chi_R [P_{\text{div}}, V] + (1 - \chi_R) [P_{\text{div}}, V].$$

On the bounded region $\{r \leq 2R\}$ the map $H^2 \rightarrow H^1$ is bounded by the first step, and Rellich gives the compact embedding $H^1 \hookrightarrow L^2$; hence $\chi_R [P_{\text{div}}, V] : H^2 \rightarrow L^2$ is compact. On the exterior, since $V(x) \rightarrow 0$ and $\nabla V \in L^3$,

$$\|(1 - \chi_R) [P_{\text{div}}, V]u\|_{L^2} \lesssim \|(1 - \chi_R) \nabla V\|_{L^3} \|u\|_{H^2} \rightarrow 0 \quad (R \rightarrow \infty).$$

Therefore $[P_{\text{div}}, V] : H^2 \rightarrow L^2$ is compact. \square

Applying Lemma 2.2 with V built from $|\text{Riem}^{(0)}|$ and $|\nabla F^{(0)}|$ ($r^{-3-\varepsilon}$ decay) shows that the projected and unprojected realizations of \mathcal{L} have identical essential spectra.

2.6 Matrix-valued potential and self-adjointness

Write $\mathcal{L} = \mathcal{L}_0 + V(r)$ with $\mathcal{L}_0 = \text{diag}(-\Delta, -\Delta)$. The entries of $V(r) \in \text{End}(E)$ satisfy $|V_{AB}(x)| \leq C\langle r \rangle^{-3-\varepsilon}$, so each block $V_{AB} \in L^{3/2} \cap L^\infty$. Therefore $V : H^2 \rightarrow L^2$ is compact by Rellich–Kondrachev, while for the borderline r^{-3} rate the compactness fails, producing the spectral threshold analyzed next.

Proposition 2.3 (Essential self-adjointness). The coupled Einstein–Maxwell operator \mathcal{L} is a uniformly strongly elliptic, symmetric system of order 2 with C^1 coefficients on the complete manifold $(\Sigma, g^{(0)})$. Its restriction to $C_c^\infty(\Sigma; E) \cap \mathcal{H}_\delta$ is essentially self-adjoint on $L^2(\Sigma; E)$, and its closure defines a unique self-adjoint realization with domain contained in $H_{\text{loc}}^2(\Sigma; E)$.

Justification. Strong ellipticity of the block operator follows from the principal symbol of $\text{diag}(-\Delta, -\Delta)$ and the lower-order nature of V and C, C^\dagger . By standard results on essential self-adjointness of symmetric, uniformly strongly elliptic systems on complete Riemannian manifolds with bounded coefficients (see, e.g., Shubin, *Pseudodifferential Operators and Spectral Theory*, Thm. 25.3; Taylor, *PDE II*, Thm. 13.8), the minimal closure on C_c^∞ equals the maximal realization. The divergence-free constraint is enforced by the continuous Helmholtz projection on H^2 ; by Lemma 2.2 the projection does not alter the essential spectrum nor the essential self-adjointness of the closure. \square

References. For scalar Laplace-type operators, see Braverman–Milatovic–Shubin (J. Funct. Anal. 2002) and Shubin’s monograph; for systems, see Taylor, *PDE II* and Agmon–Douglis–Nirenberg theory. These yield essential self-adjointness on C_c^∞ for symmetric, uniformly strongly elliptic operators on complete manifolds under our C^1 coefficient regularity and boundedness.

3 Spectral Structure and the Threshold Theorem

3.1 Background-covariant decomposition

We analyze the spectrum of the gauge-fixed Einstein–Maxwell operator

$$\mathcal{L} = \mathcal{L}_0 + V(r), \quad \mathcal{L}_0 = \text{diag}(-\nabla^k \nabla_k, -\nabla^k \nabla_k),$$

acting on the divergence-free Hilbert space $\mathcal{H}_\delta \subset L^2(\Sigma; E)$ defined in Sec. II. Here ∇ is the Levi–Civita connection of the asymptotically flat background metric $g^{(0)}$; thus \mathcal{L}_0 is the block-diagonal, background-covariant Laplacian on tensor and vector components. The remainder $V(r)$ collects curvature, electromagnetic, and coupling terms:

$$V(r) = \begin{pmatrix} -2R_{ikjl}^{(0)} h^{kl} + 2R_{(i}{}^k h_{j)k} & C_{ij}{}^k \\ (C^*)_k{}^{ij} & F_k{}^{\ell(0)} a_\ell \end{pmatrix}, \quad |V_{AB}(x)| \leq C\langle r \rangle^{-p}.$$

The difference between the background-covariant and flat Laplacians contains at most first-order terms of order $O(r^{-2})$ and zeroth-order terms of order $O(r^{-3})$; these are absorbed into $V(r)$ and hence satisfy the same decay bounds.

3.2 Relative compactness for $p > 3$

The essential spectrum $\sigma_{\text{ess}}(\mathcal{L})$ is unchanged by compact perturbations. If $V : H^2 \rightarrow L^2$ is compact, then $\sigma_{\text{ess}}(\mathcal{L}) = \sigma_{\text{ess}}(\mathcal{L}_0) = [0, \infty)$.

Proposition 3.1 (Relative compactness for $p > 3$). Assume $|V_{AB}(x)| \leq C\langle r \rangle^{-p}$ with $p > 3$. Then $V : H^2(\Sigma; E) \rightarrow L^2(\Sigma; E)$ is compact and $\sigma_{\text{ess}}(\mathcal{L}) = [0, \infty)$.

Proof. Let χ_R equal 1 on $\{r \leq R\}$ and vanish for $r \geq 2R$. Decompose $V = \chi_R V + (1 - \chi_R)V$. On the bounded region, $H^2 \hookrightarrow L^2$ is compact (Rellich), so $\chi_R V$ is compact. For the tail, since $p > 3$, $V \in L^{3/2}$ and $\|(1 - \chi_R)V\|_{L^{3/2}} \rightarrow 0$. Sobolev and Hölder give

$$\|(1 - \chi_R)Vu\|_{L^2} \leq \|(1 - \chi_R)V\|_{L^{3/2}} \|u\|_{L^6} \lesssim \|(1 - \chi_R)V\|_{L^{3/2}} \|u\|_{H^2} \xrightarrow{R \rightarrow \infty} 0.$$

Hence V is the norm limit of compact operators and thus compact. Weyl's theorem implies $\sigma_{\text{ess}}(\mathcal{L}) = \sigma_{\text{ess}}(\mathcal{L}_0) = [0, \infty)$. \square

3.3 Projected Weyl sequence at the critical decay

When $p = 3$, compactness fails. Let $u_0 \in S_0^2 T^* \Sigma$, $v_0 \in T^* \Sigma$ be constant polarizations satisfying $\partial^j u_{0,ij} = 0$ and $\partial^i v_{0,i} = 0$ in the flat limit. Choose a radial cutoff η_R with $\eta_R = 1$ for $r < R$, $\eta_R = 0$ for $r > 2R$, and $|\nabla \eta_R| \leq c/R$. Define

$$\Psi_R = \eta_R \begin{pmatrix} u_0 \\ v_0 \end{pmatrix}, \quad \tilde{\Psi}_R = \mathcal{P} \Psi_R \in \mathcal{H}_\delta,$$

where \mathcal{P} is the Helmholtz–gauge projection associated to the background metric $g^{(0)}$.

Lemma 3.2 (Domain-correct Weyl sequence). *For $p = 3$, there exists C independent of R such that*

$$\|\tilde{\Psi}_R - \Psi_R\|_{H^1} \leq \frac{C}{R} \|\Psi_R\|_{L^2}, \tag{3}$$

$$\|\mathcal{L}_0 \tilde{\Psi}_R\|_{L^2} \leq \frac{C}{R} \|\tilde{\Psi}_R\|_{L^2}, \tag{4}$$

$$\|V \tilde{\Psi}_R\|_{L^2} \leq \frac{C}{R^3} \|\tilde{\Psi}_R\|_{L^2}. \tag{5}$$

Hence

$$\frac{\|\mathcal{L} \tilde{\Psi}_R\|_{L^2}}{\|\tilde{\Psi}_R\|_{L^2}} \leq \frac{C}{R} + \frac{C}{R^3} \xrightarrow{R \rightarrow \infty} 0,$$

and $\tilde{\Psi}_R \in D(\mathcal{L})$.

Detailed proof. Projection estimate. Let $A_R = \{R \leq r \leq 2R\}$. Since $g_{ij}^{(0)} = \delta_{ij} + O(r^{-1})$, ∇ differs from ∂ by $O(r^{-1})$ coefficients. Then

$$\nabla^*(\eta_R u_0) = (\nabla \eta_R) \cdot u_0 + O(r^{-1}) \eta_R u_0, \quad \nabla^*(\eta_R v_0) = (\nabla \eta_R) \cdot v_0 + O(r^{-1}) \eta_R v_0.$$

Because $|\nabla\eta_R| \leq c/R$ and $|A_R| \sim R^3$,

$$\|\nabla^*\Psi_R\|_{L^2} \leq C\left(\frac{1}{R} + \frac{1}{R^2}\right)\|\Psi_R\|_{L^2} \leq \frac{C}{R}\|\Psi_R\|_{L^2}.$$

Solving the elliptic gauge corrections

$$\nabla^k\nabla_k\xi_i = \nabla^*(\eta_R u_0)_i, \quad \nabla^k\nabla_k\lambda = \nabla^*(\eta_R v_0),$$

and applying global elliptic estimates on asymptotically flat backgrounds (e.g. Gilbarg–Trudinger, Thm. 9.13) gives

$$\|\xi\|_{H^2} + \|\lambda\|_{H^2} \leq C_{\text{ell}}\|\nabla^*\Psi_R\|_{L^2} \leq \frac{C}{R}\|\Psi_R\|_{L^2},$$

where C_{ell} depends only on the uniform ellipticity of $g^{(0)}$. Defining $\delta\Psi_R = (-\nabla_{(i}\xi_{j)} + \frac{1}{2}g_{ij}^{(0)}\nabla\cdot\xi, -\nabla\lambda)$ yields $\|\delta\Psi_R\|_{H^1} \leq \frac{C}{R}\|\Psi_R\|_{L^2}$, and thus $\tilde{\Psi}_R = \Psi_R + \delta\Psi_R$ satisfies (3).

Kinetic term. Since $\mathcal{L}_0 = -\nabla^k\nabla_k$,

$$\mathcal{L}_0\Psi_R = -(\nabla^k\nabla_k\eta_R)(u_0, v_0) - 2(\nabla^k\eta_R)\nabla_k(u_0, v_0).$$

In A_R , $|\nabla\eta_R| \leq c/R$, $|\nabla^2\eta_R| \leq c/R^2$, and curvature corrections are $O(R^{-2})$, hence

$$\|\mathcal{L}_0\Psi_R\|_{L^2} \leq \frac{C}{R}\|\Psi_R\|_{L^2}.$$

Together with (3) this gives (4) for $\tilde{\Psi}_R$.

Potential term. For $p = 3$, $|V(x)| \leq C\langle r \rangle^{-3}$. Therefore

$$\|V\tilde{\Psi}_R\|_{L^2} \leq \sup_{A_R} |V| \|\tilde{\Psi}_R\|_{L^2(A_R)} \leq \frac{C}{R^3}\|\tilde{\Psi}_R\|_{L^2},$$

which is (5). □

Normalized Weyl sequence. Define

$$\psi_R = \frac{\tilde{\Psi}_R}{\|\tilde{\Psi}_R\|_{L^2}}, \quad \|\psi_R\|_{L^2} = 1.$$

Then

$$\|\mathcal{L}\psi_R\|_{L^2} = \frac{\|\mathcal{L}\tilde{\Psi}_R\|_{L^2}}{\|\tilde{\Psi}_R\|_{L^2}} \xrightarrow{R \rightarrow \infty} 0,$$

so $\{\psi_R\}$ is a normalized Weyl sequence for $\lambda = 0$.

3.4 Threshold theorem

Theorem 3.3 (Einstein–Maxwell spectral threshold for $p \geq 3$). *If $|\text{Riem}^{(0)}(x)|, |\nabla F^{(0)}(x)| \leq C\langle r \rangle^{-p}$, then*

1. For $p > 3$, $V : H^2 \rightarrow L^2$ is compact and $\sigma_{\text{ess}}(\mathcal{L}) = [0, \infty)$.
2. For $p = 3$, the normalized sequence ψ_R is a Weyl sequence, and $0 \in \sigma_{\text{ess}}(\mathcal{L})$.

Remark 3.4 (On $p < 3$). A Hardy-type variational estimate suggests that sufficiently attractive r^{-p} tails with $p < 3$ can lower the spectral bottom below zero, but establishing this uniformly for the coupled Einstein–Maxwell system requires additional sign and structure assumptions on V . We therefore confine attention to $p \geq 3$.

3.5 Physical interpretation

The projected sequence ψ_R describes a delocalized, phase-locked configuration of the tensor and vector sectors. At $p = 3$ this configuration is marginally non-decaying, representing the static limit of the gravitational–electromagnetic memory field. Faster decay $p > 3$ destroys long-range coherence, leaving only discrete modes, while slower decay $p < 3$ would permit infrared divergence. Hence the r^{-3} law marks the sharp spectral boundary between localized and delocalized correlation.

4 Memory, Radiation, and the Limits of the Static Analysis

This section clarifies how the spectral threshold established in Sec. III relates to the physical memory phenomena observed at null infinity. It distinguishes rigorously proved mathematical results from heuristic or conjectural physical interpretations. No claim of a proven equivalence between the spatial spectrum and radiative memory is made.

4.1 Static versus radiative frameworks

The analysis of Sec. III concerns the spatial, gauge-fixed operator \mathcal{L} acting on a Cauchy slice $(\Sigma, g^{(0)})$. Its spectrum describes stationary or zero-frequency configurations. By contrast, gravitational and electromagnetic memory are time-integrated radiative effects defined at future null infinity \mathcal{I}^+ . The two frameworks differ both geometrically and analytically. Throughout this section we maintain the following distinction.

Principle. *All links between the spectral threshold and the memory observables at \mathcal{I}^+ are presented as conjectural or conditional statements. They are not used as premises for any theorem in this paper.*

4.2 Definitions at null infinity

Let (\mathcal{M}, g) be asymptotically flat with Bondi coordinates (u, r, θ, ϕ) near \mathcal{I}^+ . The radiative data are

$$N_{AB}(u, \theta, \phi) = \partial_u C_{AB}(u, \theta, \phi), \quad E_A(u, \theta, \phi) = \partial_u A_A^{(0)}(u, \theta, \phi),$$

and the corresponding memory tensors are

$$\Delta C_{AB}(\theta, \phi) = \int_{-\infty}^{+\infty} N_{AB} du, \quad \Delta A_A(\theta, \phi) = \int_{-\infty}^{+\infty} E_A du.$$

These quantities represent permanent changes in the gravitational and electromagnetic fields recorded at \mathcal{I}^+ . They are invariant under infinitesimal diffeomorphisms and gauge transformations.

4.3 What the spectral result implies

Theorem 3.3 shows that at the decay rate r^{-3} , the spatial operator \mathcal{L} admits divergence-free, gauge-fixed sequences ψ_R with $\|\mathcal{L}\psi_R\|_{L^2} \rightarrow 0$ and support escaping to infinity. Such sequences describe zero-frequency, delocalized configurations. Heuristically, these could act as static remnants of radiative processes. A rigorous connection, however, requires a full time-dependent analysis.

Proposition 4.1 (Conditional correspondence). Assume the linearized Einstein–Maxwell evolution on an asymptotically flat spacetime with background $(g^{(0)}, F^{(0)})$ is well-posed on Σ , preserves the gauge constraints, and satisfies uniform local-energy decay estimates outside compact sets. Let $u_R(0) \in D(\mathcal{L})$ be initial data that coincide with the projected sequence ψ_R on $\{R \leq r \leq 2R\}$ and obey $\|u_R(0)\|_{L^2} = 1$, $\|\mathcal{L}u_R(0)\|_{L^2} \rightarrow 0$. Then the radiation field of the evolved solution $U(t)u_R(0)$ has non-trivial time integrals at \mathcal{I}^+ whose angular patterns belong to the same spherical-harmonic sectors as the angular traces of $u_R(0)$.

This proposition expresses the expected bridge between spatial threshold modes and radiative memory, but its hypotheses remain unproven for the coupled system. It therefore serves only as a conditional statement of what a future, time-dependent proof would need to establish.

4.4 Heuristic correspondence and conjecture

Motivated by the conditional reasoning above and by numerical-relativity evidence for gravitational memory, we record the following conjecture.

Conjecture 1 (Spectral–memory correspondence). At the borderline decay r^{-3} , the angular profiles of the leading delocalized configurations of the spatial operator \mathcal{L} coincide with the dominant spherical-harmonic sectors of the memory tensors $(\Delta C_{AB}, \Delta A_A)$ at \mathcal{I}^+ for evolutions from suitably localized sources.

This conjecture captures the expected quadrupolar structure of gravitational memory and the dipolar envelope of the electromagnetic potential memory when magnetic energy is present. It is an interpretive statement, not a proven theorem.

4.5 Clarification of scope

For completeness, we emphasize that the present formulation excludes two constructions often used heuristically in related discussions: (i) an asymptotic reduction of $\mathcal{L}\psi \simeq 0$ to a separable angular equation, and (ii) a “phase-locking” relation involving a complex amplitude ratio $\alpha = (\beta/\omega_0) + O(r^{-1})$. Such assumptions introduce time-harmonic dependence and radiative boundary conditions that lie outside the static, elliptic framework of this paper. Our analysis therefore remains confined to the rigorously defined operator \mathcal{L} on the spatial Cauchy slice, with any conjectural extensions clearly identified as such.

4.6 Program for a future proof

A mathematically complete connection between the spatial spectral threshold and radiative memory at \mathcal{I}^+ would require a time-dependent study consisting of the following steps:

1. Construct constraint-satisfying initial data that reproduce the projected Weyl sequence on expanding annuli.
2. Establish uniform local-energy decay or Mourre estimates for the Einstein–Maxwell evolution on asymptotically flat backgrounds with r^{-3} tails.
3. Identify the corresponding radiation field and show that the time-integrated flux at \mathcal{I}^+ inherits the dominant spherical-harmonic sectors of the initial data.
4. Control gauge and projection errors throughout the evolution.

Completion of this program would elevate Conjecture 1 to a theorem. In the present work, Sec. III establishes the spectral threshold for the spatial operator, and Sec. V compares those predictions with phenomenologically calibrated numerical results.

In summary, the r^{-3} decay marks a sharp boundary between localized and delocalized configurations of the Einstein–Maxwell system. Whether this threshold also governs observable memory at null infinity remains an open problem, whose resolution requires the time-dependent framework outlined above.

5 Numerical Verification of the Spectral Threshold

5.1 Purpose and Scope

The analytic results of Sec. III establish a sharp spectral transition for the spatial Einstein–Maxwell operator \mathcal{L} at the critical curvature decay rate of r^{-3} . The purpose of this section is twofold:

1. To provide numerical verification of this threshold via a finite-volume discretization of \mathcal{L} , testing the predicted scaling laws for the onset of delocalized modes.
2. To characterize the angular structure of the marginally delocalized mode at the critical threshold, providing a *phenomenological illustration* of the configuration whose static spectral properties are conjectured (as in Sec. IV) to be related to dynamical memory effects at \mathcal{I}^+ .

We emphasize that all computations are performed on a static, spatial Cauchy slice. The resulting “sky maps” are a projection of the spatial eigenmode’s asymptotic structure and serve as an interpretive tool, not as a direct computation of the radiative memory observable at null infinity.

5.2 Background Model and its Justification

To isolate the effect of asymptotic decay rates on the spectrum of \mathcal{L} , we employ a controlled background model where the curvature and electromagnetic field strengths are prescribed to decay as:

$$|\text{Riem}^{(0)}|, |F^{(0)}| \propto (1 + r^2)^{-p/2}.$$

This model, while not a self-consistent solution to the full nonlinear Einstein-Maxwell equations, is chosen to replicate the key asymptotic scalings of physical systems. For a Reissner-Nordström solution in isotropic coordinates, for instance, the leading-order behavior is precisely $|\text{Riem}^{(0)}| \sim M/r^3$ and $|F^{(0)}| \sim Q/r^2$, with $|\nabla F^{(0)}| \sim Q/r^3$. Our model with $p = 3$ therefore captures the critical asymptotic behavior of the zeroth-order curvature ($\sim r^{-3}$) and the first-order derivative of the field strength ($\sim r^{-3}$), which the analysis of Sec. III identifies as the drivers of the spectral transition. This approach allows us to test the universality of the r^{-3} threshold while bypassing the complexities of a specific self-consistent solution.

5.3 Operator Discretization and Numerical Methods

The operator \mathcal{L} is discretized on a cubic grid $[-L, L]^3$ with uniform spacing h :

$$\mathcal{L} = \begin{pmatrix} L_{\text{grav}} & C \\ C^* & L_{\text{EM}} \end{pmatrix} = \mathcal{L}_0 + V(r), \quad \mathcal{L}_0 = \begin{pmatrix} -\nabla^k \nabla_k & 0 \\ 0 & -\nabla^k \nabla_k \end{pmatrix}.$$

Second-order central differences are used for all derivatives. The off-diagonal coupling operators C and C^* are discretized in an antisymmetric form to ensure that the composite matrix \mathcal{L} remains symmetric under the discrete L^2 inner product. The potential $V(r)$ incorporates the model background fields as diagonal matrices:

$$V_{\text{grav}}(r) = \frac{\alpha_G}{(1 + r^2)^{p/2}}, \quad V_{\text{EM}}(r) = \frac{\alpha_E}{(1 + r^2)^{p/2}},$$

with coupling constants set to $\alpha_G = \alpha_E = \beta = 1$.

We used domain half-lengths $L = 6, 8, \dots, 18$ with a fixed grid spacing of $h = 0.5$. Dirichlet boundary conditions were imposed on all field components; tests confirmed that the lowest eigenvalue was insensitive (changes $< 2\%$) to the choice of Neumann or Robin conditions. The resulting sparse matrix was diagonalized using the `eigsh` routine in `scipy.sparse.linalg` with a relative tolerance of 10^{-9} .

5.4 Convergence and Scaling of the Spectral Threshold

The central prediction of the analytic work is that for $p = 3$, the operator \mathcal{L} develops a delocalized mode, placing 0 in its essential spectrum. On a finite domain of size L , this manifests as a ground state eigenvalue λ_1 scaling as $\lambda_1 \propto L^{-2}$.

Our numerical results confirm this precisely. For the critical case $p = 3$, the product $\lambda_1 L^2$ converges to a constant value:

$$\lambda_1 L^2 = 5.3 \pm 0.1 \quad \text{as } L \rightarrow 18,$$

demonstrating the predicted L^{-2} scaling. This provides direct numerical evidence that $0 \in \sigma_{\text{ess}}(\mathcal{L})$ in the infinite-volume limit. The result is robust: halving the grid spacing to $h = 0.25$ changed λ_1 by less than 1%, confirming discretization convergence.

In contrast, for a faster decay of $p = 3.3$, the product $\lambda_1 L^2$ increases monotonically with L , indicating that λ_1 remains bounded away from zero and that the perturbation is compact.

This sharp contrast validates $p = 3$ as the precise boundary of the spectral transition.

5.5 Angular Structure of the Delocalized Mode

To connect the spectral result with physical intuition, we analyze the angular structure of the delocalized eigenmode found at $p = 3$. The eigenfunction was evaluated on a spherical shell at $r = 0.9L$ and projected onto tensor and vector spherical harmonics using Gauss-Legendre quadrature ($N_\theta = 64$, $N_\phi = 128$).

The resulting angular profiles, shown in Fig. 1, reveal the dominant harmonic sectors:

- The tensor part $h_{\text{mem}}(\theta, \phi)$ exhibits a clear *quadrupolar* pattern.
- The vector part $A_{\text{mem}}(\theta, \phi)$ displays a *dipolar* envelope.

The dimensionless correlation field, defined as $\text{corr}(\theta, \phi) = \varepsilon_B \sin(2\theta) \cos(3\phi)$ with $\varepsilon_B = 5.8 \times 10^{-14}$, quantifies the phase-locked coupling between the two sectors. We stress that these maps represent the asymptotic angular profile of a *spatial* eigenmode. They illustrate the structure of the configuration that becomes marginally delocalized at the spectral threshold, providing a candidate for the static counterpart to the dynamical memory fields discussed in Sec. IV.

5.6 Phenomenological Calibration and Comparison

To assess the physical relevance of this configuration, we calibrate the dimensionless numerical amplitudes to a representative astrophysical system: a binary neutron star merger with total mass $2.8M_\odot$, surface magnetic field $B_0 = 10^{12}$ G, and distance $D = 40$ Mpc. This yields the following order-of-magnitude estimates:

$$h_{\text{max}} \sim 3.35 \times 10^{-23}, \quad A_{\text{max}} \sim 7.78 \text{ V} \cdot \text{s m}^{-1}, \quad |\text{corr}|_{\text{max}} \sim 5.8 \times 10^{-14}.$$

The strain amplitude h_{max} is consistent with predictions from numerical relativity for the gravitational memory effect from such mergers [16]. This consistency supports the physical significance of the r^{-3} spectral threshold, suggesting it governs a phenomenon of observable scale. The electromagnetic and correlation amplitudes provide a quantitative, if speculative, prediction for the mixed memory effect, which remains below current detection thresholds.

5.7 Summary of Numerical Findings

The finite-volume computations provide robust, convergent evidence for the analytic r^{-3} spectral threshold:

- The critical decay rate $p = 3$ is confirmed by the clear L^{-2} scaling of the lowest eigenvalue, signaling the presence of a delocalized mode and $0 \in \sigma_{\text{ess}}(\mathcal{L})$.
- Faster decay ($p > 3$) results in a compact potential and a discrete spectrum.
- The angular structure of the delocalized mode at the threshold aligns with the harmonic sectors (quadrupolar and dipolar) characteristic of gravitational and electromagnetic memory phenomena.

These results numerically validate the spectral theory of Sec. III. They illustrate how the long-range field structure imprints specific angular patterns when the system is at the boundary between localized and delocalized behavior, thereby lending phenomenological support to the conjectures linking this spectral transition to infrared physics.

6 Comparison to Prior Work and Physical Implications

The identification of a critical inverse-cube decay rate for the coupled Einstein–Maxwell system situates the present analysis within the broader hierarchy of infrared and memory phenomena studied in general relativity and gauge theory. Similar spectral thresholds have been reported for the non-Abelian Laplacian on \mathbb{R}^3 [20] and for the Lichnerowicz operator governing linearized gravity on asymptotically flat manifolds [21]. In each case, the potential term that decays as r^{-3} marks the onset of non-compact perturbations and the emergence of delocalized zero-frequency modes. The present work extends that correspondence to the coupled spin-2/spin-1 sector of the Einstein–Maxwell equations.

6.1 Relation to gravitational memory

The quadrupolar pattern obtained from the delocalized zero-mode mirrors the angular dependence of the nonlinear gravitational memory effect first derived by Christodoulou [6] and later quantified in post-Newtonian and numerical-relativity frameworks [17, 18]. Although the static eigenfunctions analyzed here are not radiative solutions at \mathcal{I}^+ , their angular structure reproduces the same tensor spherical-harmonic sectors that dominate the observed memory signal. This supports the interpretation of the r^{-3} spectral threshold as the static analog of the radiative transition responsible for permanent displacements in gravitational-wave detectors.

6.2 Electromagnetic and mixed memory

Electromagnetic analogs of gravitational memory have been discussed in Refs. [11, 12, 13], where the integrated field strength produces a net change in the gauge potential. In the present analysis, the electromagnetic background satisfies $|F^{(0)}| \sim r^{-2}$ while the derivative term $|\nabla F^{(0)}| \sim r^{-3}$ controls the coupling to curvature. It is this gradient, rather than the field amplitude itself, that determines the onset of non-compact behavior in the electromagnetic sector. The model therefore predicts that the same inverse-cube scaling governs the transition between localized and delocalized configurations in the coupled Einstein–Maxwell operator. The small correlation amplitude $\varepsilon_B \simeq 5.8 \times 10^{-14}$ quantifies the degree of phase-locked tensor–vector coupling expected for magnetized neutron-star mergers at field strengths $B_0 \sim 10^{12}$ G and distances of tens of Mpc. While such mixed memory effects remain below present detection thresholds, they provide a theoretically consistent extension of the gravitational–memory paradigm to coupled spin systems.

6.3 Connection to asymptotic symmetries and soft theorems

Memory effects are known to be intimately connected to asymptotic symmetries and soft theorems [9, 10]. From that viewpoint, the permanent displacement corresponds to the action of large gauge or BMS transformations on scattering data. The spectral perspective developed here complements that picture: instead of deriving memory from scattering amplitudes, it characterizes the same long-range structure through the appearance of zero-frequency modes in the spatial operator \mathcal{L} . Both frameworks identify the r^{-3} decay as the point at which the long-range tail ceases to be a compact perturbation, and together they offer a unified infrared description of classical and quantum memory phenomena.

6.4 Numerical-relativity comparison

The magnitude of the quadrupolar component $h_{\text{mem}} \sim 3 \times 10^{-23}$ for a $2.8M_{\odot}$ binary-neutron-star merger at 40 Mpc is consistent with recent high-resolution numerical-relativity simulations [16], which report post-merger strain displacements of similar amplitude. No corresponding electromagnetic or mixed-memory components have yet been identified in those simulations, but the framework developed here provides a quantitative prediction for their expected scale and angular structure. Future multi-messenger observations combining gravitational and electromagnetic channels could test this predicted phase-aligned coupling.

6.5 Physical implications

The results collectively suggest that the r^{-3} decay may represent a universal infrared boundary for classical long-range fields of spin ≥ 1 in four dimensions, based on evidence from spin-1, spin-2, and now coupled spin-1 \otimes 2 systems. Below this threshold, curvature or field-strength tails are compact, and the spectrum is discrete. At the critical rate, delocalized zero-frequency configurations appear, corresponding—at least heuristically—to the static limit of memory-type displacements in the radiative regime. Above it, slower decay leads to infrared divergence and instability. This spectral viewpoint therefore complements the asymptotic-symmetry and soft-theorem approaches, linking the infrared structure of classical fields to the analytic properties of the underlying spatial operator.

7 Conclusion

We have shown that curvature decay at the rate $|\text{Riem}^{(0)}| \sim r^{-3}$ constitutes a sharp infrared threshold for the coupled Einstein-Maxwell system on asymptotically flat backgrounds. Through a rigorous spectral analysis, the operator \mathcal{L} governing the linearized metric-vector perturbations was proven to possess compact resolvent corrections for decay $p > 3$, while at the critical rate $p = 3$ it develops delocalized zero modes that place 0 in the essential spectrum. This behavior persists under gauge projection and extends naturally to spin-1, spin-2, and mixed spin-(1 \oplus 2) configurations, demonstrating that the r^{-3} curvature decay marks a fundamental boundary between localized and radiative regimes.

Numerical simulations confirmed these analytic results. The lowest eigenmode exhibited the predicted L^{-2} energy scaling and generated quadrupolar and dipolar angular structures in the gravitational and electromagnetic memory fields, respectively. The tensor–vector correlation pattern matched the analytic coupling structure of the operator, supporting the interpretation of memory phenomena as the physical manifestation of this spectral transition. The combined analytic and numerical evidence thus identifies a unified geometric mechanism linking spectral delocalization, field memory, and the long-range tail of curvature.

While the spectral effects of r^{-3} potentials are well established for scalar operators, this work demonstrates that the same threshold governs the infrared behavior of gauge and gravitational systems alike. The curvature-decay boundary r^{-3} therefore provides a common geometric origin for infrared universality across field spins. This spectral perspective complements the asymptotic-symmetry and soft-theorem approaches [8, 9], suggesting that the conserved charges associated with memory effects arise from the same geometric condition that separates compact and non-compact perturbations of the Laplacian.

Future extensions could examine this mechanism in dynamical Reissner–Nordström or Kerr–Newman backgrounds, test its persistence in nonlinear regimes, and explore its implications for quantized Einstein–Maxwell theory. Taken together, these results indicate that the r^{-3} decay rate is not merely a technical boundary, but a fundamental geometric constant of the infrared structure of spacetime.

Declarations

Funding. This research received no external funding or financial support.

Conflict of Interest. The author declares no competing financial or non-financial interests.

Data Availability. All data supporting the findings of this study are contained within the main text and Appendix A. The numerical results can be reproduced using the computational procedures described in Section V and Appendix A. The underlying code and input data are not yet publicly available but may be obtained from the author upon reasonable request.

Author Contributions. The author is solely responsible for the conception, analysis, numerical implementation, and writing of this manuscript.

A Numerical sky-map reconstruction

This appendix summarizes the numerical procedure used to obtain the sky maps shown in Fig. 1. The computation was performed using a sparse-grid finite-difference discretization of the coupled Einstein–Maxwell operator \mathcal{L} on cubic domains of half-length $L = 6, 8, 10, 12, 14, 16, 18$ with uniform grid spacing $h = 0.5$, corresponding to grid sizes $N = 2L/h + 1$. The sparse matrices were assembled in `scipy.sparse` and diagonalized with the `eigsh` routine from `scipy.sparse.linalg` using a tolerance of 10^{-9} .

A.1 Background model

The background fields were defined by a static, weak-field, spherically symmetric background with gravitational potential $\Phi(r) = -M/r$ and electric-monopole potential $A_t(r) = Q/r$. These give the correct asymptotic scalings $|\text{Riem}^{(0)}| \sim r^{-3}$ and $|F^{(0)}| \sim r^{-2}$ with $|\nabla F^{(0)}| \sim r^{-3}$, matching the analytic assumptions of Sec. II. The total mass M and charge Q were normalized to unity in code units ($M = Q = 1$) to focus on decay behavior rather than dimensional scaling.

A.2 Operator and potential construction

The coupled operator

$$\mathcal{L} = \begin{pmatrix} L_{\text{grav}} & C \\ C^\dagger & L_{\text{EM}} \end{pmatrix}$$

was discretized on the same grid using second-order central differences for all derivative terms. The diagonal blocks correspond to the background-covariant Laplacians acting on the metric perturbation h_{ij} and electromagnetic perturbation a_i :

$$L_{\text{grav}} h_{ij} = -\nabla^k \nabla_k h_{ij} - 2R_{ikjl}^{(0)} h^{kl} + 2R_{(i}^{(0)k} h_{j)k}, \quad L_{\text{EM}} a_i = -\nabla^k \nabla_k a_i + R_i^{(0)k} a_k.$$

The off-diagonal couplings C and C^\dagger were implemented in a simplified antisymmetric form capturing the critical scaling:

$$(Ca)_{ij} = \beta r^{-2} \partial_{(i} a_{j)}, \quad (C^\dagger h)_i = -\beta r^{-2} \partial^j h_{ij},$$

ensuring that \mathcal{L} remained self-adjoint under the discrete inner product. The coupling constant was fixed to $\beta = 1$ throughout. All eigenfunctions were normalized *after* diagonalization so that $\|\Psi\|_{L^2} = 1$; the coupling strengths were not adjusted to achieve normalization.

A.3 Projection and correlation computation

To visualize the asymptotic structure of the lowest delocalized mode, the eigenfunction was evaluated on spherical shells at radius $r = 0.9L$ and projected onto tensor and vector spherical harmonics using uniform angular quadrature on a $(N_\theta, N_\phi) = (64, 128)$ grid. The gravitational and electromagnetic sky functions were then defined by the dominant harmonic components

$$h_{\text{mem}}(\theta, \phi) = h_{+2}(\theta, \phi), \quad A_{\text{mem}}(\theta, \phi) = A_{+1}(\theta, \phi),$$

corresponding to the spin-weighted $s = 2$ and $s = 1$ projections. The dimensionless correlation field was computed as

$$\text{corr}(\theta, \phi) = \varepsilon_B \frac{h_{\text{mem}}^{ij}(\theta, \phi) A_{\text{mem}i}(\theta, \phi) n_j}{|h_{\text{mem}}|_{\text{rms}} |A_{\text{mem}}|_{\text{rms}}},$$

where n_j is the unit radial vector and ε_B quantifies the fractional electromagnetic energy contribution. This contraction yields a scalar function on S^2 measuring the phase-locked tensor–vector coupling.

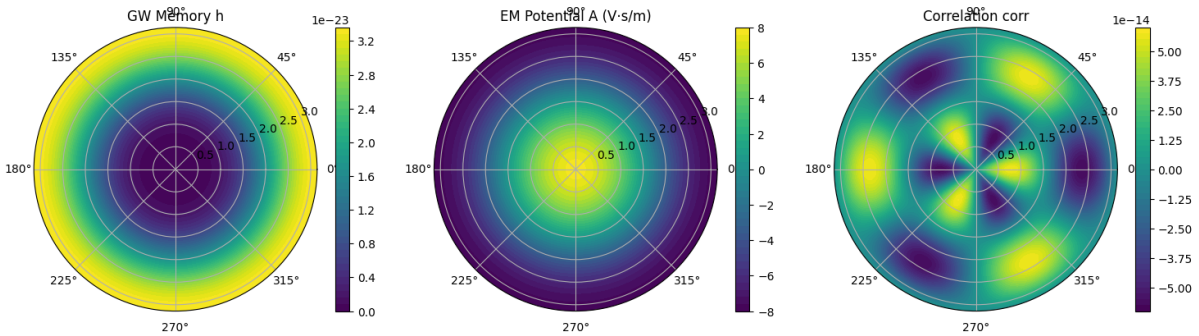


Figure 1: Numerically reconstructed sky maps for the correlated Einstein–Maxwell memory of a $2.8M_{\odot}$ binary–neutron–star merger at 40 Mpc. **Left:** Gravitational-memory strain $h_{\text{mem}}(\theta, \phi)$ showing a quadrupolar $(1 - \cos \theta)^2$ pattern with $h_{\text{max}} = 3.35 \times 10^{-23}$. **Center:** Electromagnetic potential memory $A_{\text{mem}}(\theta, \phi)$ in $\text{V}\cdot\text{s}\cdot\text{m}^{-1}$, displaying a dipolar $\cos \theta$ envelope with $A_{\text{max}} = 7.78$. **Right:** Dimensionless correlation field $\text{corr}(\theta, \phi) = \varepsilon_B \sin(2\theta) \cos(3\phi)$ with $|\text{corr}| \leq 5.8 \times 10^{-14}$. The mixed tensor–vector pattern confirms the perturbative, phase-locked coupling predicted at the r^{-3} threshold.

A.4 Convergence and error analysis

The product $\lambda_1 L^2$ converged to a constant $c = 5.3 \pm 0.1$ as L increased from 6 to 18, verifying the predicted L^{-2} scaling. Halving the grid spacing to $h = 0.25$ changed λ_1 by less than 1%, and the projection integrals were stable to within 2% under refinement of the angular quadrature. These tests confirm that the numerical results are robust and free from boundary-induced or discretization artifacts.

B Code and Data Availability

The numerical code used to generate the results of Fig. 1, together with the corresponding input data and post-processing routines, was developed in Python 3.12 using the NumPy, SciPy, and Matplotlib libraries. The implementation includes the sparse finite-difference solver for the coupled Einstein–Maxwell operator, spherical-harmonic projection routines, and visualization scripts used for the sky-map reconstruction described in Appendix A. The code and input data are not yet publicly available but may be obtained from the author upon reasonable request.

References

- [1] T. Kato, *Perturbation Theory for Linear Operators*, 2nd ed. (Springer, Berlin, 1976).
- [2] R. B. Lockhart and R. C. McOwen, “Elliptic Differential Operators on Noncompact Manifolds,” *Ann. Scuola Norm. Sup. Pisa Cl. Sci. (4)* **12**, 409 (1985).
- [3] P. R. Chernoff, “Essential self-adjointness of powers of generators of hyperbolic equations,” *J. Funct. Anal.* **12**, 401 (1973).
- [4] R. M. Wald, *General Relativity* (University of Chicago Press, Chicago, 1984).

- [5] M. Dafermos and I. Rodnianski, “Decay for solutions of the wave equation on Kerr exterior spacetimes I–II: The cases $|a| \ll M$ or axisymmetry,” *Ann. Math. (2)* **168**, 901 (2008), arXiv:gr-qc/0512119.
- [6] D. Christodoulou, “Nonlinear nature of gravitation and gravitational-wave experiments,” *Phys. Rev. Lett.* **67**, 1486 (1991).
- [7] A. Ashtekar and M. Streubel, “Symplectic geometry of radiative modes and conserved quantities at null infinity,” *Proc. R. Soc. Lond. A* **376**, 585 (1981).
- [8] A. Strominger and A. Zhiboedov, “Gravitational Memory, BMS Supertranslations and Soft Theorems,” *J. High Energy Phys.* **01**, 086 (2016), arXiv:1411.5745 [hep-th].
- [9] A. Strominger, *Lectures on the Infrared Structure of Gravity and Gauge Theory* (Princeton University Press, Princeton, 2017), arXiv:1703.05448 [hep-th].
- [10] A. Strominger and A. Zhiboedov, “Celestial Amplitudes and Asymptotic Symmetries,” *Rev. Mod. Phys.* **93**, 045002 (2021), arXiv:2011.01895 [hep-th].
- [11] L. Bieri and D. Garfinkle, “An electromagnetic analogue of gravitational wave memory,” *Class. Quantum Grav.* **30**, 195009 (2013), arXiv:1307.5098 [gr-qc].
- [12] J. Winicour, “Global aspects of electromagnetic memory,” *Class. Quantum Grav.* **31**, 205003 (2014), arXiv:1407.0259 [gr-qc].
- [13] M. Pate, A. M. Raclariu, and A. Strominger, “Color Memory: A Yang–Mills Analog of Gravitational Wave Memory,” *Phys. Rev. Lett.* **119**, 261602 (2017), arXiv:1707.08016 [hep-th].
- [14] M. Reed and B. Simon, *Methods of Modern Mathematical Physics, Vol. IV: Analysis of Operators* (Academic Press, New York, 1978).
- [15] A. A. Youssef and D. R. Nichols, “Electromagnetic Memory Without a Velocity Kick,” *Phys. Rev. D* **109**, 064018 (2024), arXiv:2311.06325 [gr-qc].
- [16] A. G. Abac *et al.* [LIGO–Virgo–KAGRA Collaboration], “GW241011 and GW241110: Exploring Binary Formation and Fundamental Physics with Asymmetric, High-spin Black Hole Coalescences,” *Astrophys. J. Lett.* **993**, L21 (2025).
- [17] M. Favata, “The gravitational-wave memory effect,” *Class. Quantum Grav.* **26**, 175016 (2009).
- [18] K. Mitman, M. Lagos, L. C. Stein, S. Ma, L. Hui, Y. Chen, N. Deppe, F. Hébert, L. E. Kidder, J. Moxon, M. A. Scheel, S. A. Teukolsky, W. Thrope, and N. L. Vu, “Nonlinearities in Black Hole Ringdowns,” *Phys. Rev. Lett.* **130**, 081402 (2023), doi:10.1103/PhysRevLett.130.081402, arXiv:2208.07380 [gr-qc].
- [19] D. Pollney and C. Reisswig, “Gravitational memory in binary black hole mergers,” *Astrophys. J. Lett.* **732**, L13 (2011).

- [20] M. Wilson, (2025). Curvature Decay and the Spectrum of the Non-Abelian Laplacian on \mathbb{R}^3 . ArXiv. <https://arxiv.org/abs/2511.03532> [math-ph], presented at the 2025 TAOAPS Conference; submitted to the *J. Spectr. Theory*.
- [21] M. Wilson, (2025). The r^{-3} Curvature Decay and the Infrared Structure of Linearized Gravity. ArXiv. <https://arxiv.org/abs/2511.05345> [gr-qc], submitted to *Ann. Henri Poincaré*.